PHILOSOPHICAL TRANSACTIONS A

royalsocietypublishing.org/journal/rsta

Research

Cite this article: VandenBussche EJ, Flannigan DJ. 2020 High-resolution analogue of time-domain phonon spectroscopy in the transmission electron microscope. *Phil. Trans. R. Soc. A* **378**: 20190598.
http://dx.doi.org/10.1098/rsta.2019.0598

Accepted: 31 May 2020

One contribution of 10 to a discussion meeting issue 'Dynamic *in situ* microscopy relating structure and function'.

Subject Areas:
materials science, electron microscopy, materials science

Keywords:
ultrafast electron microscopy, coherent acoustic phonons, *in situ* electron microscopy, gallium arsenide

Author for correspondence:
David J. Flannigan
e-mail: flan0076@umn.edu

Electronic supplementary material is available online at https://doi.org/10.6084/m9.figshare.c.5095341.

THE ROYAL SOCIETY PUBLISHING

High-resolution analogue of time-domain phonon spectroscopy in the transmission electron microscope

Elisah J. VandenBussche and David J. Flannigan

Department of Chemical Engineering and Materials Science, University of Minnesota, 421 Washington Avenue SE, Minneapolis, MN 55455, USA

DJF, 0000-0002-1829-1868

Femtosecond photoexcitation of semiconducting materials leads to the generation of coherent acoustic phonons (CAPs), the behaviours of which are linked to intrinsic and engineered electronic, optical and structural properties. While often studied with pump-probe spectroscopic techniques, the influence of nanoscale structure and morphology on CAP dynamics can be challenging to resolve with these all-optical methods. Here, we used ultrafast electron microscopy (UEM) to resolve variations in CAP dynamics caused by differences in the degree of crystallinity in as-prepared and annealed GaAs lamellae. Following *in situ* femtosecond photoexcitation, we directly imaged the generation and propagation dynamics of hypersonic CAPs in a mostly amorphous and, following an *in situ* photothermal anneal, a mostly crystalline lamella. Subtle differences in both the initial hypersonic velocities and the asymptotic relaxation behaviours were resolved via construction of space-time contour plots from phonon wavefronts. Comparison to bulk sound velocities in crystalline and amorphous GaAs reveals the influence of the mixed amorphous-crystalline morphology on CAP dispersion behaviours. Further, an increase in the asymptotic velocity following annealing establishes the sensitivity of quantitative UEM imaging to both structural and compositional variations through differences in bonding and elasticity. Implications of extending the methods and results reported here

to elucidating correlated electronic, optical and structural behaviours in semiconducting materials are discussed.

This article is part of a discussion meeting issue 'Dynamic *in situ* microscopy relating structure and function'.

Super-bandgap ultrafast photoexcitation of semiconducting materials induces a cascade of strongly correlated, many-body interactions as the system returns to the ground state [1,2]. Initial sub-picosecond generation of a dense, high-energy bath of charge-carriers transitions—typically within a few picoseconds—to atomic-scale structural responses via carrier-lattice coupling and the excitation of optical phonons. Phonon–phonon coupling then ensues over tens of picoseconds, wherein the initial population of discrete phonon states decays through the excitation of lower energy optical and acoustic modes. Resulting from this is a non-equilibrium population of propagating coherent acoustic phonons (CAPs), the precise transient behaviours of which are influenced by the intrinsic electronic and structural properties of the material, as well as the specimen boundary conditions and the manner of excitation [3–8]. Owing to the associated nanoscale structural perturbations, all-optical time-domain spectroscopic methods conducted in a pump-probe reflection geometry can be used to elucidate transient CAP responses [9]. With these techniques, depth-dependent information can be gathered and used to generate insight into underlying electronic and structural behaviours via the acousto-optic and optoelectronic properties of the material [10]. Indeed, this approach has been used to study a range of varied structures, including ion-implanted crystals and nanoporous thin films, radiation-damaged materials and polycrystalline texturing, and non-periodic structures and morphologies of plant and animal cells [11–20].

Owing to the often-discrete and heterogeneously distributed nature of the surface, interfacial, and compositional structure and morphology, combining real-space imaging with ultrafast probes would better enable determination of local transient responses and, thus, the resulting impacts on bulk intrinsic properties. All-optical techniques, such as time-domain Brillouin scattering, enable depth-dependent and in-plane imaging with nanometer and micrometre spatial resolutions, respectively [10–13,16,21,22]. While sufficient for probing structures with commensurate native length scales, imaging nanoscale in-plane dynamics and the associated impact of variable morphology and composition with these techniques is challenging. Importantly, ultrafast electron microscopy (UEM)—wherein a femtosecond laser is coupled to an otherwise conventional transmission electron microscope (TEM)—is well suited for imaging in-plane nanoscale dynamics on picosecond timescales [23–25]. Indeed, UEM has been used to directly image both in-plane and z-direction CAP dynamics (e.g. nucleation and launch, propagation and time-domain phase-velocity dispersion) with combined nanometer-picosecond spatio-temporal resolutions [4–8,26,27]. Further, ultrafast parallel- and convergent-beam diffraction can also be conducted with UEM, thus enabling correlative studies of unit-cell and nanoscale structural dynamics in reciprocal and real space, respectively, on the same specimen region [6,8,28–30].

Here, we show that the spatio-temporal capabilities of UEM can be used to differentiate the impact of amorphous and crystalline morphologies comprising semiconducting materials on time-domain CAP dispersion behaviours via imaging of nanoscale-picosecond in-plane propagating lattice perturbations. Using amorphized GaAs specimens prepared via focused ion-beam milling, subtle variations in CAP dispersion behaviours—as directly imaged with UEM—were observed following *in situ* pulsed-laser annealing and an associated increase in crystallinity. In addition to describing in detail the specific approaches taken to directly observe and quantify this behaviour, we also discuss the manner in which subtle differences in dispersion

responses manifest in space-time contour plots, while also illustrating the increased level of structural and dynamic information that can be obtained with UEM for studies such as these. We conclude by noting the implications of this work for connecting morphologically dependent electronic and optical properties of semiconductors to lattice dynamics with techniques having high spatio-temporal resolutions.

The specimens studied here were thin lamella of undoped GaAs prepared from bulk crystals via focused ion-beam (FIB) milling (see the Materials and methods section for preparation details). This archetypal semiconductor was chosen for study because it is known to support coherent optical and acoustic phonons that may have non-trivial connections to coherent charge-carrier phenomena [31,32]. In addition, the elastic properties are known to be dependent upon the degree of amorphization caused, for example, by ion bombardment and implantation, as occurs during FIB milling [33]. Indeed, surface amorphization is a well-known consequence of FIB milling, which leads to the formation of both amorphous and polycrystalline damaged layers on the exposed faces of the lamella surrounding a region of higher crystallinity [34,35]. Electron diffraction patterns from such specimens display relatively sharp Bragg spots together with significant diffuse-scattering signal arising from the damage layers (figure 1*a*). Following *in situ* photothermal annealing of such a specimen, during which the overall degree of crystallinity in the damage layers is increased, associated diffraction patterns show a commensurate decrease in the diffuse-scattering signal (figure 1*b–e*; see the Materials and methods section for *in situ* photothermal annealing details). From here forward, Bragg scattering, Bragg peaks and Bragg spots shall all refer to the relatively sharp Bragg spots observed in the patterns, while any reference to diffuse scattering or diffuse signal shall refer to the relatively diffuse ring arising from the FIB-damaged layers. Note that, while referred to as amorphous, it may be more accurate to classify the damaged layers as consisting of randomly oriented nanocrystallites (ignoring any possible texturing). Regardless, differentiation of these two types of signal and classification of the morphologies as relatively crystalline and relatively amorphous is adequate for the purposes of the work described here.

The relative degree of crystallinity of the lamella before and after *in situ* photothermal annealing can be estimated from selected-area electron diffraction (SAED) patterns [36]. Here, this was essentially done by isolating the Bragg-scattered intensity from the total intensity via azimuthally averaging over select regions of the pattern containing the spots. This was followed by subtracting the Bragg intensity from the total signal once the underlying diffuse signal was quantified and removed. Bragg-spot intensity was isolated by least-squares fitting with a Gaussian peak-fitting algorithm [37]. This effectively extracts the diffuse-scattering signal so that direct comparison of the associated intensities of the pre- and post-annealed specimen can be made. A detailed description of the method used to isolate and differentiate the amorphous and crystalline signals is given in the electronic supplementary material. Here, following this method, per cent crystallinity was calculated from the pre- and post-annealed specimen patterns (figure 1) and was determined to be $23 \pm 4\%$ and $79 \pm 2\%$, respectively, where uncertainties are one standard deviation over five repetitions of the analysis.

Direct imaging of CAP dynamics with UEM is possible due to the combination of high spatio-temporal resolutions (routinely nanometer-picosecond) and the sensitivity of diffraction contrast to slight changes in the overlap of the reciprocal lattice for thin foils and the Ewald sphere when at or near a Bragg-scattering condition [38–40]. Here, UEM bright-field imaging was used to quantify CAP dynamics in the pre- and post-annealed GaAs lamella for direct comparison. For reference, the FIB-damaged outer layers of the lamella surrounded an inner relatively crystalline layer, and the incident electron wavevector was perpendicular to the lamella surfaces. Additional details of the UEM CAP experiments are given in the Materials and methods section, and other pertinent but generally applicable information is published elsewhere [4–7,27,41]. Following *in situ* femtosecond photoexcitation, coherent contrast waves arising from excitation of CAPs were observed in both the pre- and the post-annealed GaAs lamella. Figure 2 shows an illustrative summary of the CAP dynamics observed and quantified

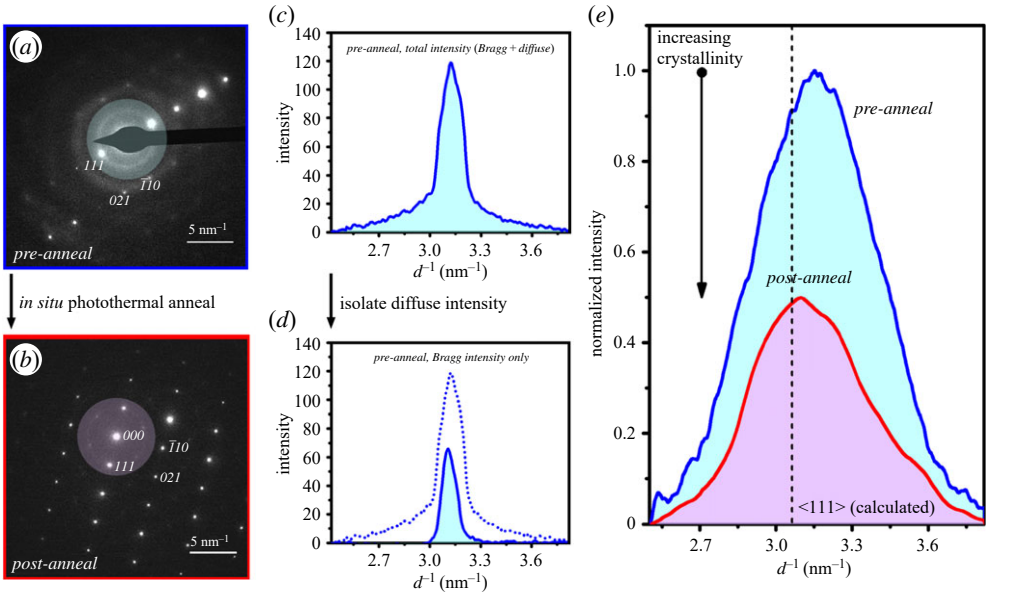

Figure 1. *In situ* photothermal anneal of a GaAs lamella. (*a*) Selected-area electron diffraction (SAED) pattern of a pre-annealed GaAs specimen viewed along the [11$\bar{2}$] crystallographic zone axis. Three Bragg spots are indexed for reference. The light cyan disk marks the approximate region of the pattern that was azimuthally averaged to obtain the profiles shown in subsequent panels. (*b*) SAED pattern of the post-annealed specimen viewed along the [11$\bar{2}$] zone axis. The *000* beam is indexed for reference, and the light magenta disk marks the approximate azimuthally averaged region. (*c*) Total-intensity profile (Bragg and diffuse) of the pre-annealed specimen. (*d*) Bragg-only intensity profile (solid blue line and light cyan fill) of the pre-annealed specimen. The total-intensity profile shown in (*c*) (blue dotted line) is included for comparison. (*e*) Illustrative comparison of the pre- and the post-annealed diffuse-only intensity at the same observed scattering vector as the *<111>* planes (calculated position shown for reference). Peak shifts from the calculated position may arise from residual tensile strain or a slight systematic error in the calibration of the microscope. (Online version in colour.)

in the pre-annealed specimen (figure 2*a* for a representative UEM bright-field image; see also electronic supplementary material, video S1). Similar results were obtained for the post-annealed specimen (not shown; see electronic supplementary material, video S2) but with a different time-varying phase-velocity (v_p) dispersion behaviour arising from differences in the elastic constants (described below and in the electronic supplementary material). Though the individual phonon wavefronts produce an elastic unit-cell distortion that is likely on the order of a few picometers or less, orientation near or at a Bragg-scattering condition (i.e. near or at an existing bend contour) ultimately gives rise to an associated coherent, oscillatory contrast response due to modulation of the excitation error [5,38,40]. In this way, CAP behaviours, such as emergence, propagation velocities (figure 2*b*,*c*) and v_p dispersion, can be quantitatively tracked.

Key to differentiating CAP behaviours for pre- and post-annealed GaAs specimens is the quantification of the time-varying v_p dispersion behaviours for each. The method for extracting this information from a UEM bright-field image series is summarized in figure 3. Following the establishment of a rectangular region of interest (ROI) oriented with the long axis parallel to the phonon propagation direction (see the electronic supplementary material for details), average-intensity image profiles for each UEM temporal snapshot in the series are generated (figure 3*a*–*c*). The width of the ROI is set such that a balance is struck between maximizing the signal-to-noise ratio and preserving the nature of the extent of the wavefront. Individual phonon wavefronts are identifiable as depressions in the profile counts arising from an increase in Bragg-scattered intensity for the reasons described above. Progress of each individual phonon across the ROI can then be tracked by combining the spatial intensity profiles together to form a space-time contour plot (STCP; figure 3*d*). This procedure allows tracking of phonon movement with few-pixel (i.e.

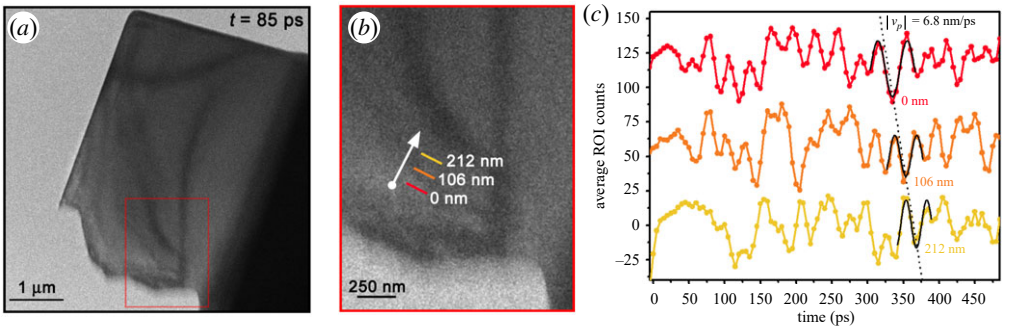

Figure 2. Demonstration of UEM imaging of CAPs in a free-standing, pre-annealed GaAs lamella. (*a*) Representative UEM bright-field image at $t = 85$ ps (i.e. 85 ps after *in situ* photoexcitation). The red rectangle indicates the region within which phonon dynamics were tracked and quantified. (*b*) Magnified view of the select region shown in (*a*). Three select positions (coloured lines) at which average image counts were monitored are shown. Relative positions of the lines are labelled, with the position of the red line set as the origin. The white arrow indicates the observed direction of the propagating phonon wavetrain. (*c*) Average region-of-interest (ROI) image counts at the select positions shown in (*b*) as a function of time. Propagation of a single representative phonon wavefront is highlighted with the dotted line to exemplify how velocity can be determined from such profiles. The wavefront arrives at the 106 nm and 212 nm markers approximately 16 ps and 31 ps, respectively, after passing the origin (0 nm), thus indicating a phase-velocity magnitude, $|v_p|$, of 6.8 nm ps^{-1} for this particular phonon. The fits straddling the dotted line are simple undamped sine functions and are meant to highlight the localized oscillatory response arising from the individual phonon wavefront. (Online version in colour.)

10 nm at the magnification used here) precision. Figure 3 (*e*,*f*) shows a representative UEM image of a pre-annealed GaAs specimen, a select ROI positioned within a section displaying active CAP dynamics (see the electronic supplementary material, videos) and the resulting STCP. Individual phonon behaviours manifest as dark, linear features in the STCP, from which v_p can be extracted by determining the slope, the magnitude of which is then plotted as a function of time (figure 3*g*), thus revealing the dispersion behaviour [5]. The data are fit with a single-exponential decay curve to extract an asymptotic phase velocity, $v_{p,0}$ (equation 1).

$$v_p = Ae^{(-t/\tau)} + v_{p,0} \tag{0.1}$$

Here, A is a pre-exponential, τ is a decay constant and t is time. See the electronic supplementary material for more details and for descriptions of various control experiments.

It is worth noting that while the STCP analyses performed here were conducted on a single, select ROI, an inspection of the electronic supplementary material videos shows that CAPs were in fact initiated and launched from each vacuum-specimen interface, or lamella edge, following *in situ* photoexcitation. This indicates that the direction of CAP propagation is not dependent upon crystallographic orientation. Instead, acoustic-phonon launch from morphological features, such as step-edges and interfaces, is hypothesized to arise from a rapid dephasing of directional phonon modes due to inherent differences in the interfacial boundary conditions at such features and the associated influence on the lattice response following photoexcitation [6]. Indeed, rapid dephasing of CAPs caused by crystal step-edges that are a single unit cell in height has been observed with UEM [7]. Further, the CAPs imaged here are hypothesized to be Lamb waves, as has been observed in single-crystal, undoped Ge [4,5]. Such guided-wave modes generally display multiple orders in the frequency domain, most of which have hypersonic phase velocities with strong dispersion behaviours. However, it remains an open question as to why single-mode excitation appears to occur here and also in previous UEM studies [5]. Further, the observed single-exponential decay of v_p in the time domain (figure 3*g*) is subject to several explanations, such as enhanced carrier screening during charge-carrier equilibration and cooling [5,31].

Using the methods described above, CAP time-domain dispersion behaviours for the pre- and post-annealed GaAs specimen shown in figure 1 were determined with UEM imaging (figure 4).

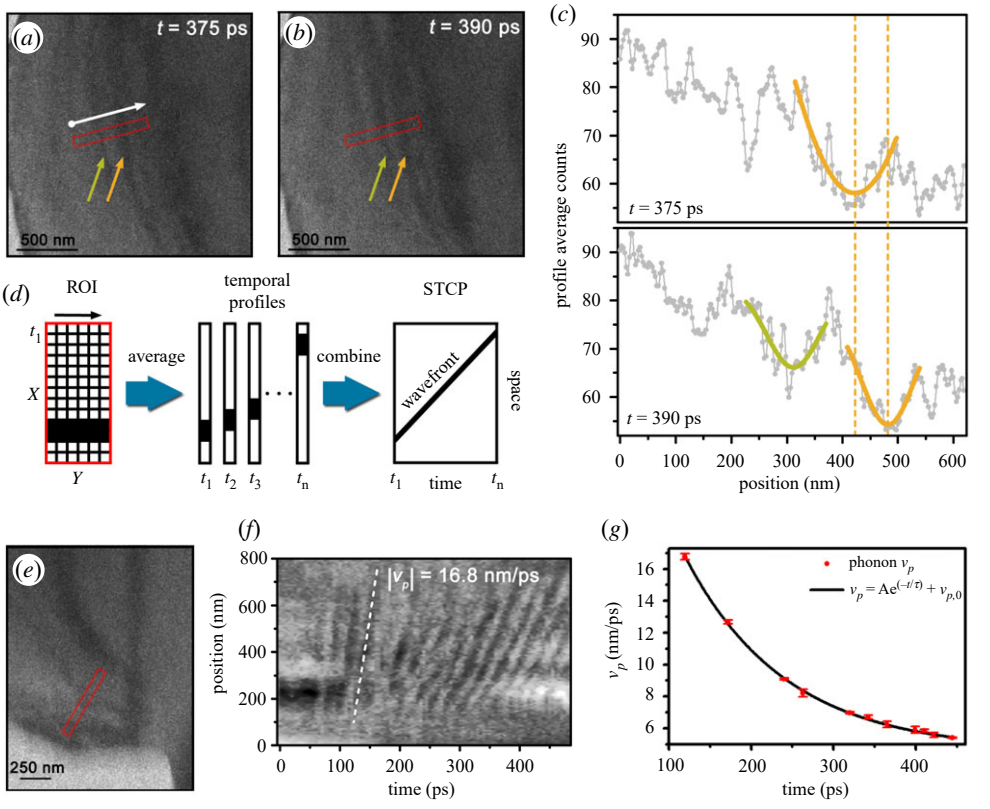

Figure 3. Dynamics and dispersion of CAPs from UEM imaging. (*a*,*b*) Representative UEM bright-field images of a GaAs lamella at $t = 375$ ps (*a*) and $t = 390$ ps (*b*) showing the presence of contrast bands arising from propagating CAPs. The red rectangles mark the position of an ROI from which contrast profiles were acquired, as shown in (*c*). The coloured arrows highlight two individual CAP wavefronts, and the white arrow indicates the propagation direction. (*c*) ROI profiles from the UEM images shown in (*a*) (upper plot) and (*b*) (lower plot). Wavefronts produce a drop in average counts owing to increased scattering strength and are fit with a peak function to quantify position with time (coloured inverted peak fits to the data). The dashed vertical lines spanning both plots mark the position of a select wavefront and illustrate the propagating nature of the contrast feature. (*d*) Concept of the generation of a space-time contour plot (STCP) from the ROI profiles. For each UEM image in a temporal series (e.g. t_1, t_2, etc. where each time point is an individual snapshot), counts are averaged along one spatial dimension of a two-dimensional ROI to produce a temporal intensity profile with one spatial dimension. These profiles are then combined into an STCP, where single wavefronts appear as sloped lines revealing speed and direction (i.e. velocity, *v*). (*e*) Select UEM image with ROI indicated (red rectangle), from which the STCP shown in (*f*) was generated. (*f*) STCP spanning from $t = -5$ ps to 485 ps. Each dark band is a phonon wavefront (the position of a select wavefront is indicated with the white dashed line). The $|v_p|$ of the marked wavefront is 16.8 nm ps^{-1}. (*g*) Time-domain v_p dispersion behaviour determined via STCP analysis from a UEM image series. Only dark bands which could be accurately fit are included; more details can be found in the electronic supplementary material. Error bars on the data points are one standard deviation of the average of 10 repetitions of the analysis procedure for the same data. (Online version in colour.)

Methods for ensuring that CAP dynamics could be directly compared across the pre- and post-annealed specimen are described in the electronic supplementary material. For reference, the specific phonon wavetrains analysed were each found to propagate approximately along the [$\bar{1}$31] crystallographic direction, as determined with correlative imaging and diffraction (see the electronic supplementary material). As noted above, however, the particular crystallographic direction does not dictate CAP propagation direction. Here, the determination of the wavetrain propagation direction with respect to crystallographic orientation was done in order to provide a common reference for the compared CAP behaviours. As can be seen in figure 4, CAPs in

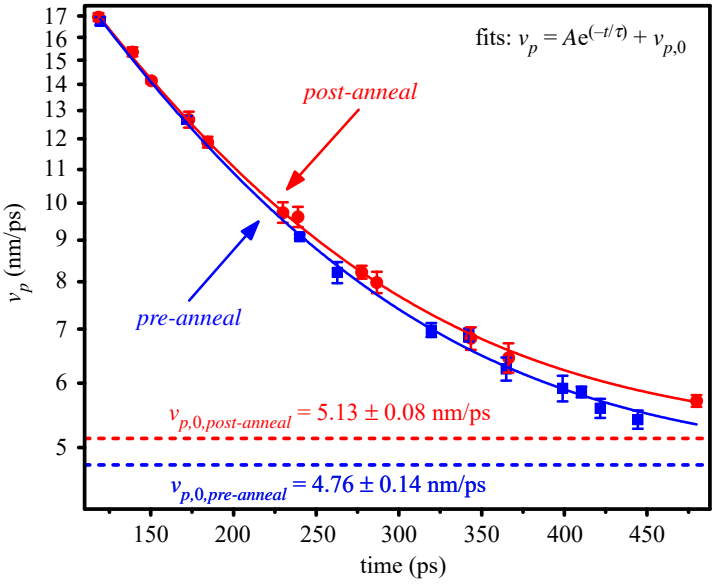

Figure 4. Time-dependent phase velocity (v_p) for pre- and post-annealed GaAs (blue squares and red dots, respectively). The data are fit (solid curves) with the single-exponential decay function shown in the upper-right corner of the plot. The asymptotes for each curve ($v_{p,0}$) are indicated with horizontal, coloured dashed lines, and the values determined from the fit are shown. The error bars on the data points are one standard deviation of the average of 10 separate fits of the wavefront peaks in the associated STCPs (not shown), and errors on the asymptotic values for $v_{p,0}$ are one standard error of fits to the v_p data. (Online version in colour.)

both the pre- and post-annealed specimen display hypersonic phase velocities that exponentially decay to the range of longitudinal speeds of sound in GaAs. Importantly, however, the final asymptotic velocity values ($v_{p,0}$) differ; in the pre-annealed state, $v_{p,0} = 4.76 \pm 0.14\,\mathrm{nm\,ps^{-1}}$, while $v_{p,0} = 5.13 \pm 0.08\,\mathrm{nm\,ps^{-1}}$ in the post-annealed state, thus giving an increase in CAP velocity of $0.37 \pm 0.15\,\mathrm{nm\,ps^{-1}}$ upon annealing and increased specimen crystallinity. The $v_{p,0}$ error values are standard errors of the fit of the exponential decay function to the data, while that of the difference is a propagated error. As is the case for the data in figure 3*g*, error bars on the data points in figure 4 are one standard deviation of 10 repetitions of the entire STCP fitting procedure.

The observed difference in $v_{p,0}$ for the pre- and post-annealed specimen indicates that a change in morphology—namely an increase in relative crystallinity—is the source of the difference and that UEM CAP imaging is sensitive to such variations. Comparison of the values of $v_{p,0}$ determined here to those for entirely crystalline and entirely amorphous GaAs is informative. The longitudinal speed of sound in the $[\bar{1}31]$ direction for crystalline GaAs is estimated to be $5.4\,\mathrm{nm\,ps^{-1}}$ [33]. By comparison, it is expected that an amorphous specimen would support a significantly reduced speed of sound of $3.8\,\mathrm{nm\,ps^{-1}}$, as estimated from the associated elastic constants (see the electronic supplementary material for details). Here, both the pre- and post-annealed state are some combination of the crystalline and amorphous structure as a consequence of the FIB-preparation method used and the resulting damage layers. Though calculation of the precise dispersion behaviours in such a structure is non-trivial and beyond the scope of this work, the experimentally observed behaviour in figure 4 is in agreement with that expected for both a mixed morphology (i.e. between the two $v_{p,0}$ extremes) and a post-anneal increase in crystallinity (i.e. a commensurate increase in $v_{p,0}$).

Measurable differences between the asymptotic $v_{p,0}$ values for an as-prepared and an annealed specimen raises the question of whether it is generally possible to use UEM to access additional material information by measurement of phonon phase velocities. Indeed, acoustic-wave behaviour has been used to study a broad range of optical phenomena and discrete structures,

including the effect of heterostructure architectures and ion implantation on optical refraction, the structures of buried layers and interfaces, the constants associated with deformation potential, and the properties of bond stiffness and elasticity [13,14,42–46]. Accordingly, combining the relatively high-spatio-temporal resolution of UEM imaging with modelling and controlled specimen geometries and compositions may lead to significant improvements in precision and accuracy, as well as to new insights into structure–function relationships via correlative methods (e.g. ultrafast imaging, diffraction and spectroscopy). In particular, significant impacts may be made on improving understanding of the influence of discrete nanoscale structures and morphologies—especially at both exposed and buried interfaces—on emergent optical and electronic properties of semiconducting materials.

In summary, we have described a method based on UEM bright-field imaging for quantifying coherent acoustic-phonon dynamics, especially the time-domain dispersion behaviours that manifest in the thin lamella of archetypal semiconducting materials like GaAs and Ge. We have shown that the combined nanometer-picosecond spatio-temporal resolution of UEM imaging can be used to isolate and differentiate subtle differences in dynamics induced by changes in specimen structure and morphology. In particular, the high-resolution aspects of UEM relative to all-optical spectroscopic methods enable access to higher order structural and temporal information, with correlative unit-cell and nanoscale studies potentially leading to a broader understanding of the underlying physical principles at work. We envision that extension of the methods described here to systems of increasing complexity and highly varied composition will lead to new insights into semiconductor heterostructures and buried epitaxial interfaces, highly beam-sensitive hybrid materials with sensitive compositional constraints, and engineered nanostructured materials for carrier-transport optimization.

Materials and methods

(a) Specimen preparation and *in situ* photothermal anneal

The GaAs lamella was prepared from a bulk, undoped *100*-oriented GaAs crystal (MTI Corporation) using FIB milling and a lift-out procedure (FEI Helios NanoLab G4 dual-beam FIB). The resulting lamella (100 nm thick) was beam-welded to a TEM Cu mesh grid in the FIB and was oriented along the [11$\bar{2}$] zone axis (i.e. the incident electron wavevector in the electron microscope was parallel to the [11$\bar{2}$] crystallographic direction). The FIB-prepared GaAs lamella was photothermally annealed *in situ* using a diode-pumped, solid-state Yb : KGW pulsed-laser (Light Conversion PHAROS, 300-fs pulse duration full-width at half-maximum, fwhm). Pulse duration was measured with a scanning autocorrelator (Light Conversion GECO). The train of laser pulses was directed onto the specimen via alignment through an optical periscope integrated into the side of the UEM (more on the UEM instrument below). The repetition rate (50 kHz; 20 µs between pulses) and pulse fluence (35 mJ/cm^2; estimated spot size of 120 µm, fwhm) used to anneal the specimen were such that complete thermal dissipation between pulses did not occur, thus resulting in an elevated steady-state temperature (see the electronic supplementary material for an experiment that confirmed this). The laser wavelength was 515 nm ($h\nu = 2.4$ eV) generated with a harmonics module (Light Conversion HIRO).

(b) Ultrafast electron microscopy instrumentation and coherent acoustic-phonon imaging experiments

The UEM instrument at the University of Minnesota consists of a conventional thermionic TEM modified for ultrafast operation (FEI Tecnai Femto, Thermo Fisher) and the same femtosecond pulsed laser used for *in situ* photothermal annealing (described above). The UEM was operated at 200 kV in pump-probe, bright-field imaging mode for the CAP experiments. The pump beam consisted of 515 nm wavelength pulses of 300 fs duration (fwhm), with an estimated spot size

on the specimen of 120 µm fwhm and a resulting fluence of 0.75 mJ/cm^2. The probe consisted of discrete electron packets generated via the photoelectric effect by directing 258 nm wavelength laser pulses onto a graphite-encircled, 50-µm diameter, truncated LaB_6 cathode (Applied Physics Technologies). Here, the electron packets contained an average of 80 electrons each at the detector, and the CAP imaging experiments were conducted at a repetition rate of 20 kHz (50 µs between pulses/packets) with an acquisition time per image of 10 s. The arrival time between the pump laser pulse and the probe electron packet is controlled with a linear-bearing mechanical delay stage (Aerotech PRO165LM). All images and diffraction patterns were acquired with a 16 megapixel CMOS camera modified for continuous operation (Gatan OneView). Further information about the Ultrafast Electron Microscopy Lab at the University of Minnesota can be found elsewhere [4,5,7,8]. The UEM videos reported here spanned from either −5 ps or −10 ps to 485 ps, with a step-size of 5 ps. Here, 0 ps is defined as experimental time zero, or the first moment when dynamics are detected, which may be different from true time zero (i.e. the moment of femtosecond photoexcitation) [5].

Data accessibility. Data has been uploaded to the Data Repository of the University of Minnesota and can be freely accessed at this link: http://hdl.handle.net/11299/212097 or via the https://doi.org/10.13020/36wa-rj64.

Authors' contributions. E.J.V. contributions were formal analysis, investigation, methodology, software, validation, visualization, writing—original draft, writing—review and editing. D.J.F. contributions were conceptualization, formal analysis, funding acquisition, methodology, project administration, resources, supervision, visualization, writing—original draft, writing—review and editing.

Competing interests. The author(s) declare that they have no competing interests.

Funding. This material is based on work supported by the U.S. Department of Energy, Office of Science, Office of Basic Energy Sciences under Award No. DE-SC0018204. This material is based upon work supported by the National Science Foundation Graduate Research Fellowship Program under Grant No. DGE-1348264. Part of this work was carried out in the College of Science and Engineering Characterization Facility, University of Minnesota, which has received capital equipment funding from the NSF through the UMN MRSEC program under Award Number DMR-2011401.

References

1. Othonos A. 1998 Probing ultrafast carrier and phonon dynamics in semiconductors. *J. Appl. Phys.* **83**, 1789–1830. (doi:10.1063/1.367411)
2. Axt VM, Kuhn T. 2004 Femtosecond spectroscopy in semiconductors: a key to coherences, correlations and quantum kinetics. *Rep. Prog. Phys.* **67**, 433–512. (doi:10.1088/0034-4885/67/4/r01)
3. Ruello P, Gusev VE. 2015 Physical mechanisms of coherent acoustic phonons generation by ultrafast laser action. *Ultrasonics* **56**, 21–35. (doi:10.1016/j.ultras.2014.06.004)
4. Cremons DR, Plemmons DA, Flannigan DJ. 2016 Femtosecond electron imaging of defect-modulated phonon dynamics. *Nat. Commun.* **7**, 11230. (doi:10.1038/Ncomms11230)
5. Cremons DR, Du DX, Flannigan DJ. 2017 Picosecond phase-velocity dispersion of hypersonic phonons imaged with ultrafast electron microscopy. *Phys. Rev. Mater.* **1**, 073801. (doi:10.1103/PhysRevMaterials.1.073801)
6. Cremons DR, Plemmons DA, Flannigan DJ. 2017 Defect-mediated phonon dynamics in TaS_2 and WSe_2. *Struct. Dyn.* **4**, 044019. (doi:10.1063/1.4982817)
7. Zhang Y, Flannigan DJ. 2019 Observation of anisotropic strain-wave dynamics and few-layer dephasing in MoS_2 with ultrafast electron microscopy. *Nano Lett.* **19**, 8216–8224. (doi:10.1021/acs.nanolett.9b03596)
8. Reisbick SA, Zhang Y, Flannigan DJ. 2020 Influence of discrete defects on observed acoustic–phonon dynamics in layered materials probed with ultrafast electron microscopy. *J. Phys. Chem. A* **124**, 1877–1884. (doi:10.1021/acs.jpca.9b12026)
9. Rogers JA, Maznev AA, Banet MJ, Nelson KA. 2000 Optical generation and characterization of acoustic waves in thin films: Fundamentals and applications. *Annu. Rev. Mater. Sci.* **30**, 117–157. (doi:10.1146/annurev.matsci.30.1.117)
10. Gusev VE, Ruello P. 2018 Advances in applications of time-domain Brillouin scattering for nanoscale imaging. *Appl. Phys. Rev.* **5**, 031101. (doi:10.1063/1.5017241)

11. Steigerwald A *et al.* 2009 Semiconductor point defect concentration profiles measured using coherent acoustic phonon waves. *Appl. Phys. Lett.* **94**, 111910. (doi:10.1063/1.3099341)
12. Mechri C, Ruello P, Breteau JM, Baklanov MR, Verdonck P, Gusev V. 2009 Depth-profiling of elastic inhomogeneities in transparent nanoporous low-k materials by picosecond ultrasonic interferometry. *Appl. Phys. Lett.* **95**, 091907. (doi:10.1063/1.3220063)
13. Steigerwald A, Hmelo AB, Varga K, Feldman LC, Tolk N. 2012 Determination of optical damage cross-sections and volumes surrounding ion bombardment tracks in GaAs using coherent acoustic phonon spectroscopy. *J. Appl. Phys.* **112**, 013514. (doi:10.1063/1.4732072)
14. Gregory J, Steigerwald A, Takahashi H, Hmelo A, Tolk N. 2012 Ion implantation induced modification of optical properties in single-crystal diamond studied by coherent acoustic phonon spectroscopy. *Appl. Phys. Lett.* **101**, 181904. (doi:10.1063/1.4765647)
15. Yarotski D, Fu E, Yan L, Jia Q, Wang Y, Taylor AJ, Uberuaga BP. 2012 Characterization of irradiation damage distribution near $TiO_2/SrTiO_3$ interfaces using coherent acoustic phonon interferometry. *Appl. Phys. Lett.* **100**, 251603. (doi:10.1063/1.4729621)
16. Nikitin SM, Chigarev N, Tournat V, Bulou A, Gasteau D, Castagnede B, Zerr A, Gusev VE. 2015 Revealing sub-μm and μm-scale textures in H_2O ice at megabar pressures by time-domain Brillouin scattering. *Sci. Rep.* **5**, 9352. (doi:10.1038/srep09352)
17. Kuriakose M *et al.* 2016 Picosecond laser ultrasonics for imaging of transparent polycrystalline materials compressed to megabar pressures. *Ultrasonics* **69**, 259–267. (doi:10.1016/j.ultras.2016.03.007)
18. Danworaphong S *et al.* 2015 Three-dimensional imaging of biological cells with picosecond ultrasonics. *Appl. Phys. Lett.* **106**, 163701. (doi:10.1063/1.4918275)
19. Pérez-Cota F, Smith RJ, Moradi E, Marques L, Webb KF, Clark M. 2015 Thin-film optoacoustic transducers for subcellular Brillouin oscillation imaging of individual biological cells. *Appl. Opt.* **54**, 8388–8398. (doi:10.1364/ao.54.008388)
20. Pérez-Cota F, Smith RJ, Moradi E, Marques L, Webb KF, Clark M. 2016 High resolution 3D imaging of living cells with sub-optical wavelength phonons. *Sci. Rep.* **6**, 39326. (doi:10.1038/srep39326)
21. Ramanathan S, Cahill DG. 2006 High-resolution picosecond acoustic microscopy for non-invasive characterization of buried interfaces. *J. Mater. Res.* **21**, 1204–1208. (doi:10.1557/jmr.2006.0141)
22. Lomonosov AM, Ayouch A, Ruello P, Vaudel G, Baklanov MR, Verdonck P, Zhao L, Gusev VE. 2012 Nanoscale noncontact subsurface investigations of mechanical and optical properties of nanoporous low-k material thin film. *ACS Nano* **6**, 1410–1415. (doi:10.1021/nn204210u)
23. Zewail AH. 2010 Four-dimensional electron microscopy. *Science* **328**, 187–193. (doi:10.1126/science.1166135)
24. Flannigan DJ, Zewail AH. 2012 4D electron microscopy: Principles and applications. *Acc. Chem. Res.* **45**, 1828–1839. (doi:10.1021/ar3001684)
25. Plemmons DA, Suri PK, Flannigan DJ. 2015 Probing structural and electronic dynamics with ultrafast electron microscopy. *Chem. Mater.* **27**, 3178–3192. (doi:10.1021/acs.chemmater.5b00433)
26. Kwon O-H, Barwick B, Park HS, Baskin JS, Zewail AH. 2008 Nanoscale mechanical drumming visualized by 4D electron microscopy. *Nano Lett.* **8**, 3557–3562. (doi:10.1021/nl8029866)
27. McKenna AJ, Eliason JK, Flannigan DJ. 2017 Spatiotemporal evolution of coherent elastic strain waves in a single MoS_2 flake. *Nano Lett.* **17**, 3952–3958. (doi:10.1021/acs.nanolett.7b01565)
28. Barwick B, Park HS, Kwon O-H, Baskin JS, Zewail AH. 2008 4D imaging of transient structures and morphologies in ultrafast electron microscopy. *Science* **322**, 1227–1231. (doi:10.1126/science.1164000)
29. Yurtsever A, Zewail AH. 2009 4D nanoscale diffraction observed by convergent-beam ultrafast electron microscopy. *Science* **326**, 708–712. (doi:10.1126/science.1179314)
30. Feist A, da Silva NR, Liang W, Ropers C, Schäfer S. 2018 Nanoscale diffractive probing of strain dynamics in ultrafast transmission electron microscopy. *Struct. Dyn.* **5**, 014302. (doi:10.1063/1.5009822)
31. Hu BY-K, Stanton CJ, Wilkins JW. 1991 Acoustic mode with time-dependent phase velocity in photoexcited semiconductors. *Phys. Rev. B* **44**, 11 067–11 071. (doi:10.1103/PhysRevB.44.11067)

32. Kutt WA, Albrecht W, Kurz H. 1992 Generation of coherent phonons in condensed media. *IEEE J. Quantum Electron.* **28**, 2434–2444. (doi:10.1109/3.159550)
33. Mutti P, Sklar Z, Briggs GAD, Jeynes C. 1995 Elastic properties of GaAs during amorphization by ion implantation. *J. Appl. Phys.* **77**, 2388–2392. (doi:10.1063/1.358763)
34. Rubanov S, Munroe P. 2001 Investigation of the structure of damage layers in TEM samples prepared using a focused ion beam. *J. Mater. Sci. Lett.* **20**, 1181–1183. (doi:10.1023/A:1010950201525)
35. Kato NI. 2004 Reducing focused ion beam damage to transmission electron microscopy samples. *J. Electron Microsc.* **53**, 451–458. (doi:10.1093/jmicro/dfh080)
36. An B-S, Kwon Y, Cha H-W, Kang M-C, Oh J-S, Yang C-W. 2019 Quantification of crystallinity using zero-loss filtered electron diffraction. *Microsc. Res. Tech.* **82**, 39–46. (doi:10.1002/jemt.23065)
37. VandenBussche EJ, Flannigan DJ. 2019 Reducing radiation damage in soft matter with femtosecond-timed single-electron packets. *Nano Lett.* **19**, 6687–6694. (doi:10.1021/acs.nanolett.9b03074)
38. Cremons DR, Schliep KB, Flannigan DJ. 2013 Diffraction contrast as a sensitive indicator of femtosecond sub-nanoscale motion in ultrafast transmission electron microscopy. *Proc. SPIE* **8845**, 884507. (doi:10.1117/12.2023145)
39. VandenBussche EJ, Flannigan DJ. 2019 Sources of error in Debye-Waller-effect measurements relevant to studies of photoinduced structural dynamics. *Ultramicroscopy* **196**, 111–120. (doi:10.1016/j.ultramic.2018.10.002)
40. Du DX, Flannigan DJ. 2020 Imaging phonon dynamics with ultrafast electron microscopy: kinematical and dynamical simulations. *Struct. Dyn.* **7**, 024103. (doi:10.1063/1.5144682)
41. Valley DT, Ferry VE, Flannigan DJ. 2016 Imaging intra- and interparticle acousto-plasmonic vibrational dynamics with ultrafast electron microscopy. *Nano Lett.* **16**, 7302–7308. (doi:10.1021/acs.nanolett.6b03975)
42. Duggal AR, Rogers JA, Nelson KA. 1992 Real-time optical characterization of surface acoustic modes of polyimide thin-film coatings. *J. Appl. Phys.* **72**, 2823–2839. (doi:10.1063/1.351535)
43. Liu R, Sanders GD, Stanton CJ, Kim CS, Yahng JS, Jho YD, Yee KJ, Oh E, Kim DS. 2005 Femtosecond pump-probe spectroscopy of propagating coherent acoustic phonons in $In_xGa_{1-x}N/GaN$ heterostructures. *Phys. Rev. B* **72**, 195335. (doi:10.1103/physrevb.72.195335)
44. Ogi H, Fujii M, Nakamura N, Shagawa T, Hirao M. 2007 Resonance acoustic-phonon spectroscopy for studying elasticity of ultrathin films. *Appl. Phys. Lett.* **90**, 191906. (doi:10.1063/1.2737819)
45. Hettich M, Jacob K, Ristow O, He C, Mayer J, Schubert M, Gusev V, Bruchhausen A, Dekorsy T. 2012 Imaging of a patterned and buried molecular layer by coherent acoustic phonon spectroscopy. *Appl. Phys. Lett.* **101**, 191606. (doi:10.1063/1.4767141)
46. Mante P-A, Stoumpos CC, Kanatzidis MG, Yartsev A. 2017 Electron–acoustic phonon coupling in single crystal $CH_3NH_3PbI_3$ perovskites revealed by coherent acoustic phonons. *Nat. Commun.* **8**, 14398. (doi:10.1038/ncomms14398)